PCCP

Accepted Manuscript

ROYAL SOCIETY OF CHEMISTRY

www.rsc.org/pccp

Journal Name

RSCPublishing

ARTICLE

Bio-inspired Design of Electrocatalysts for Oxalate Oxidation: a Combined Experimental and Computational Study of Mn-N-C Catalyst

Cite this: DOI: 10.1039/x0xx00000x

Received 00th January 2012,
Accepted 00th January 2012

DOI: 10.1039/x0xx00000x

www.rsc.org/

Ivana Matanovic,[a,b] Sofia Babanova[a], Albert Perry III[a] , Alexey Serov[a], Kateryna Artyushkova[a] and Plamen Atanassov[a]

We report a novel non-Platinum Group Metal (non-PGM) catalyst derived from Mn and amino-antipyrinine (MnAAPyr) that shows electrochemical activity towards oxidation of oxalic acid comparable to Pt with an onset potential for oxalate oxidation measured at 0.714 ± 0.002 V vs. SHE at pH=4. The material has been synthesized using a templating Sacrificial Support Method with manganese nitrate and 4-aminoantipyrine as precursors. The catalyst is a nano-structured material in which Mn is atomically dispersed on a nitrogen-doped graphene matrix. XPS studies reveal high abundance of pyridinic, Mn–N_x, and pyrrolic nitrogen pointing towards the conclusion that pyridinic nitrogen atoms coordinated to manganese constitute the active centers. Thus, the main features of the MnAAPyr catalyst exhibit similarity with the active sites of naturally occurring enzymes that are capable of efficient and selective oxidation of oxalic acid. Density Functional Theory in plane wave formalism with Perdew, Burke and Ernzerhof functional was further used to study the stability and activity of different one-metal active centers that could exist in the catalyst. The results show that the stability of the Mn-N_x sites changes in following order: MnN_4 > MnN_3C > MnN_2C_2 > MnN_3. Based on the overpotentials of 0.64 V and 0.71 V vs. SHE, calculated using the free energy diagrams for oxalate oxidation mechanism, we could conclude that the MnN_3C and MnN_2C_2 sites are most probable Mn-N_x sites responsible for the reported catalytic activity of the new catalyst.

Introduction

Oxalic acid is a metabolite, which is of critical importance to living organisms. It is also a highly stable "poly-oxo-fuel", a derivative of incomplete and non-selective oxidation of glycerol of other biofuels. Its oxidation, or electrooxidation can be a critical step in technologies aiming the introduction of bio-derived fuels into electrochemical power generation through fuel cells or redox flow batteries. The importance of oxalic acid is also widely recognized in food and water technology and clinical diagnosis. Small carboxylic or dicarboxylic acids (such as formic, maleic, and acetic acids) are intermediate products in catalytic oxidation of aromatic compounds present in wastewater [1]. At the same time oxalic acid is a compound that is toxic to almost all organisms. The accumulation of oxalic acid causes hyperoxaluria, formation of calcium oxalate stones in the kidney, renal failure, cardiomyopathy, and cardiac conductance disorders[1-3].

Electrochemical oxidation of organic compounds is a commonly used approach for wastewater purification[4], energy production[5-7], and synthesis of value added products[8]. Metal oxides, like copper, zinc, manganese and supported noble metals, such as platinum group metals (PGM) or zinc, are used as catalysts in these processes due to their high activity and lack of selectivity[9-14]. Platinum and ruthenium carbon supported catalysts are shown to be efficient for the oxidation of different carboxylic acids. For example, oxalic acid can be oxidized using platinum in mild experimental conditions, pH = 0 and potential values between 0.7 and 1.8 V vs. RHE with a maximum catalytic activity at 1.3 V[15]. Unfortunately, the use of noble metal catalysts such as platinum group metals is expensive, which hinders their large-scale application for wastewater purification. Additionally, in metal-catalyzed oxidation there is a risk of irreversible deactivation due to the modifications of the metal surface in the course of reactions by metal sintering or poisoning of the surface by strongly adsorbed species, such as oxygen. Metal leaching in the solution is another known problem when composite metal oxides are used[1, 15]. At the same time numerous redox enzymes, mainly oxidases and dehydrogenases, are capable of fast, efficient, and selective oxidation of complex and simple organic compounds. These enzymes are capable of not only pollutants removal, but can use electrochemical oxidation of organic compounds to gain energy.

Three main types of enzymes are recognized as capable of oxalate oxidation. These are oxalate oxidase (OxOx), oxalate decarboxylase (OxDC) and oxalyl-CoA synthetase[16-18]. Among them OxOx and OxDC have similar active centers although the products of oxalate transformation are not the same. OxOx oxidizes oxalic acid to carbon dioxide and hydrogen peroxide (Eq. (1)), while OxDC produces formate and CO_2 (Eq. (2)) [16].

$$C_2H_2O_4 + O_2 \rightarrow 2CO_2 + H_2O_2 \quad Eq.(1)$$

$$C_2H_2O_4 \rightarrow HCOOH + CO_2 \quad Eq.(2)$$

Both enzymes are manganese-containing enzymes. Each monomer of the hexamer OxOx has one active center with Mn (II) incorporated in it. OxDC is a trimer and each monomer unit has two Mn-binding sites. In both enzymes Mn (II)/Mn (III) is identified as the redox pair associated with the enzyme activity and oxalate oxidation[16, 18].

The enzymes' high redox activity is a result of years of evolutionary improvements of their structure and function. A key characteristic is the specifically designed active center supported by the surrounding amino acid residues and enzyme tertiary structure. Although highly active and selective, the efficient utilization of enzymatic systems as catalysts in various electrochemical processes is still problematic due the enzymes' short life and a limited range of environmental conditions they are able to operate in[19, 20]. However, the development of more robust inorganic catalysts by mimicking the enzyme active center provides a new avenue in the development of materials electrochemically active for oxidation of organic compounds.

In this study we developed a novel heterogeneous electrocatalyst inspired by the structure of the active site of Mn-binding site of oxalate oxidase and oxalate decarboxylase. The synthesized catalyst belongs to the family of M-N-C catalysts also referred as non-platinum group metals (non-PGMs) based catalysts[21-24]. It is commonly accept today that in such catalysts the transition metal (Fe or Co in most literature examples) is coordinated by nitrogen-containing defects in a graphene-like matrix. Such "ligand-like" environment is proving for a molecular nature of the heterogeneous catalysts structure and is the critical prerequisite for the bio-inspired catalyst design. The synthesis approach was based on modified Sacrificial Support Method (SSM) developed at University of New Mexico[5-8, 14, 21, 24-28] for materials that are based on Fe-N-C family. These catalysts demonstrate very good activity towards oxygen reduction, but have never been tested as catalyst for the oxidation of organic compounds, including oxalic acid. In addition, we used density functional theory (DFT) to model the possible active sites of the catalysts and discussed the reactivity of the catalyst based on the calculated free energy diagrams for oxalate oxidation on these centers.

Experimental Section

Catalysts synthesis

The non-PGM catalyst used in this study, abbreviated here as Mn-AAPyr, was synthesized using manganese nitrate and 4-aminoantipyrine (AAPyr) as precursors. The synthesis was based on the Sacrificial Support Method where silica (Cab-O-Sil™ LM150, ~200 $m^2 g^{-1}$) was used as a support material, which provides porosity of the catalyst at the macro scale. Initially, a dispersion of silica (metal loading on silica was calculated to be 25 wt%) into acetone was obtained by using a low-energy ultrasonic bath. Separately, a solution of 4-aminoantipyrine (Sigma-Aldrich) in acetone was prepared and added to the silica colloidal solution. The silica-AAPyr suspension was ultrasonicated for 40 minutes. A solution of Mn (II) nitrate ($Mn(NO_3)_2$*$4H_2O$, Sigma-Aldrich) in distilled water was then added to the silica-AAPyr solution and ultrasonicated for about 8 hours. The gel formed containing silica-Mn-AAPyr was dried for 12 hours at controlled temperature (85°C) and then grounded to a fine powder using a mortar and pestle. The following step was a heat treatment with temperature ramp rate of 25°C per minute from room temperature to 950°C, followed by pyrolysis for 30 minutes. The heat treatment was done in Ultra High Purity (UHP) nitrogen with a flow rate of 100 ml min^{-1}. Finally, silica sacrificial support was removed using hydrofluoric acid (HF 20 wt.%) and the catalyst was then washed with distilled water until neutral pH and dried for 12 hours at controlled temperature (85°C).

Ink preparation

Ink composed of MnAAPyr and Nafion was prepared as follows: 2 mg MnAAPyr were suspended in 370 µl of water:IPA mixture (4:1 ratio, reagent grade, Sigma, St. Louis, MO) with the addition of 30 µl 0.5 % Nafion and bath ultasonicated for 30min.

Electrochemical studies

The activity of the designed catalyst towards the oxidation of oxalic acid was studied using three-electrode setup. The working electrode was glassy carbon rotating disk electrode onto which 20 µl of the prepared ink (See the above section) were drop casted and dried under ambient conditions. Saturated Ag/AgCl was used as a reference and Pt-wire as a counter electrode. The electrolyte was composed of 0.1M potassium phosphate buffer at pH 4. To increase the conductivity of the solution 0.1M KCl was introduced as indifferent electrolyte. Cyclic voltammetry (CV) was carried out by sweeping the potential between -0.8 and 1.4 V vs. saturated Ag/AgCl electrode, with a scan rate of 10 mV/s in absence and presence of 0.1 M oxalic acid. The CV in the absence of oxalic acid was used as a control sample. All potentials in the paper are reported vs. SHE and were calculated by adding 0.197 V to the potential measured using saturated Ag/AgCl electrode as a reference electrode.

XPS analysis

XPS spectra were acquired on a Kratos Axis DLD Ultra X-rayphotoelectron spectrometer using an Al Kα source monochromatic operating at 150 W with no charge compensation. The base pressure was about 2×10^{-10} Torr, and operating pressure was 2×10^{-9} Torr. Survey and high-resolution spectra were acquired at pass energies of 80 and 20 eV respectively. Data analysis and quantification were performed using CasaXPS software. A linear background subtraction was used for quantification of C1s, O1s and N1s spectra, while a Shirley background was applied to Mn2p spectra. Sensitivity factors provided by the manufacturer were

utilized. A 70% Gaussian/30%Lorentzian line shape was utilized in the curve-fit of N1s.

Computational methods

All electronic structure calculations were performed using generalized gradient approximation (GGA) to Density Functional Theory (DFT) with the Perdew-Burke-Ernzerhof (PBE) functional[29, 30] and projector augmented-wave pseudopotentials[31, 32] as implemented in Vienna Ab initio Software Package (VASP)[33-36]. The electronic energies were calculated using 3x3x1 k-point Monkhorts-Pack[37] mesh and tetrahedron method with Blöchl corrections [38]. In all the cases, plane-wave basis cutoff was set to 700 eV. Extended surfaces were modeled using super-cells with the dimensions of 17.04 Å x 17.04 Å, γ = 60° and a vacuum region of 20 Å. Using this approach optimized extended graphene structure has C-C distance of 1.42 Å, which is in agreement with previous experimental observations for graphite [39]. Active sites of MnAAPyr were modeled by removing one carbon atom from the graphene in the case of MnN_3 and two adjacent carbon atoms in the case of MnN_4, MnN_3C, and MnN_2C_2 sites, respectively. The resulting internal edges are substituted with 3N atoms in the case of MnN_3 and MnN_3C sites, 4N atoms in the case of MnN_4 site, and 2N atoms in the case of MnN_2C_2 site. The structures were further coordinated to the manganese atom and were allowed to relax until the convergence in energy was $1x10^{-5}$ eV. The lattice was kept fixed at the DFT optimized value for graphene. In the case of MnN_2C_2 sites, two possible coordination of manganese were considered; one in which manganese atom is coordinated with nitrogen atoms that are adjacent to each other, and the other in which manganese is coordinated with nitrogen atoms that are opposite to each other (Fig. 1). Formation energies of proposed active sites of MnAAPyr were calculated based on the following set of reactions:

$$C_{n-\text{graphene}} \rightarrow C_{n-1} + C \quad (3a)$$

$$C_{n-1} \rightarrow C_{n-2} + C \quad (3b)$$

$$C_{n-2} + \frac{m}{2}N_2 \rightarrow N_mC_{n-2} + mC \quad (4a)$$

$$C_{n-1} + \frac{m}{2}N_2 \rightarrow N_mC_{n-1} + mC \quad (4b)$$

$$N_mC_{n-2} + Mn \rightarrow MnN_mC_{n-2} \quad (5a)$$

$$N_mC_{n-1} + Mn \rightarrow MnN_mC_{n-1} \quad (5b)$$

which sums to the final formation reaction

$$C_{n-\text{graphene}} + \frac{m}{2}N_2 + Mn \rightarrow MnN_mC_{n-x} + C_x \quad (6)$$

where x is 1 or 2. Energy changes in each of the steps were calculated using the change in the electronic energy for the appropriate system. $C_{n\text{-graphene}}$, $N_mC_{n\text{-}x}$, and $MnN_mC_{n\text{-}x}$ correspond to the energies of pristine graphene sheet, optimized graphene with $N_mC_{n\text{-}x}$ defects, and optimized $N_mC_{n\text{-}x}$ defects with manganese atoms incorporated, respectively. For electronic energies of carbon, nitrogen, and manganese we used total energy per carbon atom for defect free graphene, half of the total energy of N_2 molecule, and total energy of an isolated manganese atom in gas phase. Due to the exploratory nature of this work, only the formation energy terms in Eq (6) were computed i.e. the zero point energy and entropy corrections were not included. However, the changes in entropy are expected to be of the same order when comparing different defects and are therefore unlikely to significantly change the reported results[40].

The mechanism of oxalic acid oxidation on the five considered active sites was further studied using DFT approach. The steps in the oxalic acid oxidation mechanism considered in this study are given in Eq. (9) and include transfer of two electrons directly from oxalic acid molecule to the catalyst surface. The change in the Gibbs free energy for all the steps in the mechanism were calculated using equation:

$$\Delta_r G = \Delta E + \Delta\text{ZPE} - T\Delta S \quad (7)$$

where ΔE is the change in the electronic energy during the reaction, ΔZPE is the change in the zero-point energy, and ΔS is the change in the entropy. ZPE values were calculated using the vibrational frequencies obtained from the normal mode analysis and entropy changes were obtained from standard molecular tables [41]. By the use

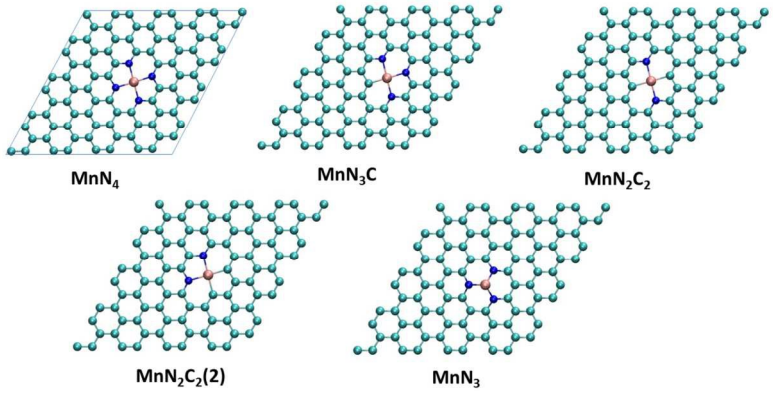

Figure 1. Computationally optimized structures of sites considered as actives sites for oxalate oxidation in MnAAPyr. One unit cell is shown.

of the standard hydrogen electrode, the chemical potential for proton/electron pair is related to that of the ½ H_2(g) and the energy difference for the reaction *A + H^+ + e^- → *AH was, under standard conditions, calculated as the free energy change for the reaction *A+½ H_2 → *AH [42, 43].

At finite pH and potential, the free energy change of the reaction becomes:

$$\Delta_r G = \Delta E + \Delta \mathrm{ZPE} - T\Delta S - neU - k_B T ln10\mathrm{pH} \quad (8)$$

Where n is the number of electrons exchanged in the reaction and U is the electrode potential.

The docking of oxalic acid and oxalic anion on OxOx was modeled using AutoDock Vina 4 [44]. The geometries of oxalic acid and oxalic anions in water were first optimized using MP2/6-311++G(d,p) level of theory and polarizable continuum solvation model as implemented in Gaussian09 [45].

Results and Discussion

The developed catalyst, abbreviated here as MnAAPyr, is a member of non-PGM M-N-C family of materials. It has been synthesized using Sacrificial Support Method (SSM) [25], which was developed in our group to synthesize different materials: oxides, carbon-based materials, ORR catalysts, etc. Along with its low cost, the main advantage of this catalyst is its high catalytic surface area i.e. the active sites of the material are situated within its own structure, turning it into a highly porous framework with high density of active sites.

Catalyst morphology

Morphological analysis of MnAAPyr catalyst by TEM (Fig. 2 left) revealed highly graphitic three-dimensional graphene-like structure typical for catalysts synthesized by SSM. The TEM image also indicates heterogeneous morphology, as it was further seen by SEM analysis. SEM showed highly developed 3D open-frame, sponge-like structure of the catalyst (Fig. 2 right) with two types of pores: pores with diameter ~60-90 nm created after removal of the sacrificial support, and smaller pores ~10-15 nm formed during the decomposition of the precursor.

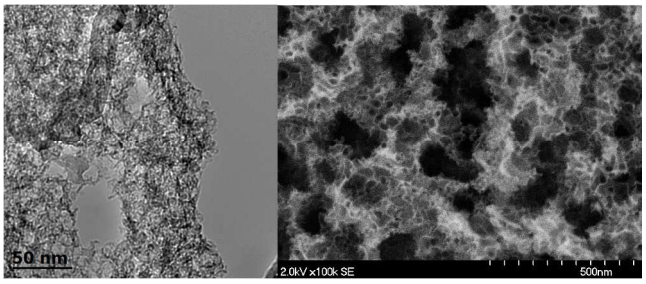

Figure 2: TEM (left) and SEM (right) images of MnAAPyr.

Surface chemistry

The XPS analysis of the synthesized MnAAPyr has shown the presence of 7.4 % of nitrogen and 0.2 % of manganese (Table 1). The N1s spectrum (Figure 3 left) consists of the following major types (above 20%) of N: pyridinic (398.8 eV), Mn–N_x (399.8 eV), and pyrrolic (401 eV). In previous studies nitrogen atoms coordinated to metal and pyridinic nitrogen have been suggested to be active sites for ORR [21, 46]. The high abundance of these types of nitrogens points towards the same conclusion of pyridinic N and Mn-N_x coordination being a part of active centers. Mn 2p spectra (Figure 3b) show two major peaks due to manganese associated with nitrogen (Mn-N_x) and oxygen, such as MnO_2 and satellite peaks due to MnOx.

Table 1 summarizes the results of the XPS analysis. The averages of three areas are shown.

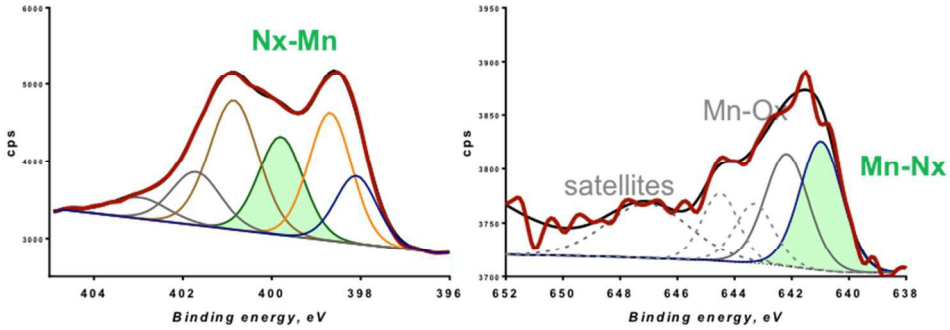

Figure 3: XPS high-resolution N1s (left) and Mn2p (right) spectra.

Table 1: XPS data for MnAAPyr catalyst.

Sample	C 1s %	O 1s %	N 1s %	Mn 2p %	N cyano %	N pyrid %	N-Mn %	N pyrrolic %	N qua %	N graph %	Mn-N %	MnO_2 %
Mn AAPyr 1	87.6	4.4	7.8	0.2	12.3	24.1	19.2	27.8	11.4	5.2	52.8	47.2
Mn AAPyr 2	86.7	5.9	7.2	0.2	11.6	24.4	20.5	27.1	11.4	5.0	57.9	42.1
Mn AAPyr 3	87.0	5.6	7.2	0.1	10.7	24.8	20.8	27.0	11.6	5.2	47.1	52.9
	87.1	**5.3**	**7.4**	**0.2**	**11.5**	**24.4**	**20.2**	**27.3**	**11.5**	**5.1**	**52.6**	**47.4**

Electrochemical performance

The activity of the MnAAPyr catalyst towards oxalate oxidation was studied using cyclic voltammetry at pH 4 (Fig. 4). The pH was selected based on the optimal pH for oxalate oxidation through enzymatic catalysis[16, 18]. At pH = 4, oxalic acid is partially deprotonated (pKa_1 = 1.23 and pKa_2 = 4.19) [41]. Therefore in the electrolyte oxalic acid along with oxalic anions will be present.

Comparing the anodic currents in absence and presence of 0.1M oxalic acid it can be concluded that at pH = 4 MnAAPyr is electrochemically active towards the oxidation of oxalic acid. The onset potential of the redox transformation of the oxalate was found to be 0.714 ± 0.002 V vs. SHE. This onset potential is similar to the potential of 0.700 V vs. RHE at which oxalate oxidation on platinum was observed in highly acidic media (pH < 1)[15], which is 4 times lower pH than the one in the current study. It is also known that the Pt activity regarding oxalate oxidation is pH dependent and decreases at higher pHs[15, 47]. Thus the developed herein catalyst shows lower overpotential towards oxalate oxidation in comparison to Pt.

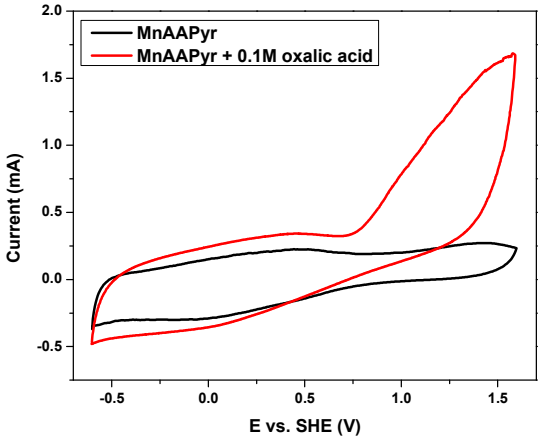

Figure 4: Cyclic voltammetry of MnAAPyr in phosphate buffer, pH 4 at 10 mV/s.

On the CV of MnAAPyr in phosphate buffer before and after the addition of oxalic acid two broad redox peaks were recorded. The oxidation peak appeared at 0.470 ± 0.010 V, followed by a reduction peak at 0.048 ± 0.003 V vs. SHE. The presence of these peaks indicates a redox couple with formal redox potential of 0.259 ± 0.004 V vs. SHE. Based on possible redox states, this redox couple could be Mn^{3+}/Mn^{2+} or Mn^{4+}/Mn^{3+} [48, 49]. The generated currents due to the oxidation of oxalic acid on MnAAPyr are comparable with the currents obtained using Pt, a benchmark catalyst, at pH 1 and 1000 rpm [47] and even higher than the currents recorded at platinum single crystal electrodes [50].

Computational calculations

DFT calculations were used to study the structure and formation energy of the various Mn-N_x active sites in which manganese is assumed to be coordinated with two, three, or four nitrogen atoms[51]. The formation energies and optimized geometries of MnAAPyr proposed active sites are given in Table 2 and Figure 1. Formation energies were calculated as -2.50 eV, -1.30 eV, 0.14 eV, 0.03 eV and 0.30 eV for MnN_4, MnN_3C, MnN_2C_2, $MnN_2C_2(2)$ and MnN_3 sites, respectively. According to these results, formation of MnN_4 and MnN_3C sites is energetically favorable, while the formation of other sites is energetically unfavorable with the formation of $MnN_2C_2(2)$ sites still plausible at high temperatures. Furthermore, the stability of the sites is predicted to change in the following order: MnN_4 > MnN_3C > $MnN_2C_2(2)$ > MnN_2C_2 > MnN_3. MnN_4 active site is predicted to be the most stable, while MnN_3 site is predicted to be the least stable site, which would imply that this site would also be the least occurring site in our material. However, absolute values of formation energies calculated in Table 2 depend on both initial and final states of species in Eq. (6), which makes comparison with the material prepared with SSM method somewhat difficult. The state of the carbon before or after its removal from the initial material will play a role in determining calculated values of formation energies of different defect sites in MnAAPyr[52]. In addition, from a theoretical point of view bulk bcc Mn would represent a better choice for the reference state of manganese than the atomic Mn. Using PBE functional, it was calculated that Mn(g) lies 3.7 eV above the bcc Mn, which would change the values in the fourth column of the Table 2 for a constant factor of +3.7 eV. However, as the source of manganese in the synthesis process was Mn(II) nitrate, it is considered that this reference state would lead to systematic underestimation of the MnAAPyr formation energies.

Analysis of the energy changes in the individual steps (3)-(5) can provide more information on the stability and the occurrence of different sites in MnAAPyr. We have to note that we do not consider

reactions (3)-(5) as consecutive steps in the formation mechanism, but rather as individual steps that can provide us with more insight on the formation energetics. Reactions (3a) and (3b) consider the defect formation steps, which are the removal of one or two carbon atoms from the infinite graphene sheet. Steps (4a) and (4b) consider addition of N_2 to substitute carbon atoms along the edges of defects with nitrogen atoms, and steps (5a) and (5b) represent the incorporation of Mn in the catalysts defects.

Table 2. Formation energies in eV of proposed active sites for MnAAPyr as calculated using DFT with PBE functional (reactions (3)-(6)).

Active site	Eq. (4a)	Eq. (5a)	Eq. (4a)+(5a)	Eq. (3a)+(3b)+(4a)+(5a)
MnN_4	-3.29	-6.53	-9.82	-2.50
MnN_3C	-1.74	-6.88	-8.62	-1.30
MnN_2C_2	-0.16	-7.02	-7.18	+0.14
$MnN_2C_2(2)$	-0.04	-7.25	-7.29	+0.03
	Eq. (4b)	**Eq. (5b)**	**Eq. (4b)+(5b)**	**Eq. (3b)+(4b)+(5b)**
MnN_3	-4.16	-3.29	-7.45	+0.30

Formation energies of single and double atom vacancy sites in Eq. (3a) and (3b) were calculated as 7.75 eV and -0.43 eV. As predicted previously, formation of single or double atom vacancies in pristine graphene is energetically unfavorable [52-54]. Substituting edge carbon atoms with nitrogen atoms stabilizes the defect sites, and the stabilization effect is more pronounced for less stable single atom vacancies. For example, substituting three carbon atoms with nitrogen along the edge in single vacancy defect site induces an energy change of -4.16 eV, while the energy change of -1.74 eV is calculated if the same number of nitrogen atoms gets introduced along the edges of a double atom vacancy defect. Incorporation of Mn further stabilizes the N-containing defect sites in MnAAPyr. The effect is more pronounced for less stable N-containing defects, such as N_2C_2 defects than for more stable N-containing defects, such as N_3C or N_4 defects. Interestingly, incorporation of Mn to form MnN_3 sites, induces N atoms to move out from the graphene plane for 0.42 Å resulting in trigonal pyramid coordination of Mn (Fig. 5 right). Similar coordination of Mn by nitrogen is observed in the active center of oxalate oxidase and oxalate decarboxylase[16], where in OxOx Mn (II) is partially coordinated by three N-atoms from three histidine residues (His 88, His 90 and His 137) forming Mn-binding site (Fig. 5 left). The out of plane position of Mn relative to the three N-atoms shows similarity with MnN_3 active site of MnAAPyr although in the enzyme's active center Mn is also coordinated by Glu 95 and two water molecules, which accounts for the octahedral coordination of Mn. In all other MnAAPyr active centers N and Mn atoms are situated in the graphene plane and Mn is coordinated by nitrogen or carbon atoms in square planar geometry. If we assume that the substitution of carbon with nitrogen and incorporation of Mn proceeds in carbon based material with existing single and double atoms defects, calculated formation energies become -9.82 eV, -8.62 eV, -7.18 eV, -7.29 eV, and -7.45 eV for MnN_4, MnN_3C, MnN_2C_2, $MnN_2C_2(2)$ and MnN_3 sites, respectively. This indicates somewhat larger stability of MnN_3 sites than predicted based on Eq (6), however, these sites are still less energetically stable than MnN_4 or MnN_3C sites. In conclusion, based on the DFT energetics we can suggest that MnN_4 and MnN_3C sites are expected to be predominantly occurring sites in MnAAPyr with less frequent MnN_2C_2, $MnN_2C_2(2)$, and MnN_3 sites. The conclusion based on the DFT calculations correlates with the observations done through XPS analyses of other M-N-C materials showing M-N_4 as the most abundant M-N_x species [46]. Note that at high temperatures, such as the ones reached during the synthesis, an increase in entropy can compensate the loss in formation energy and additionally stabilize all the defect sites [40]. However, it is difficult to predict the concentrations of different sites in the real material without explicitly including the entopic term, which was beyond the scope of this work.

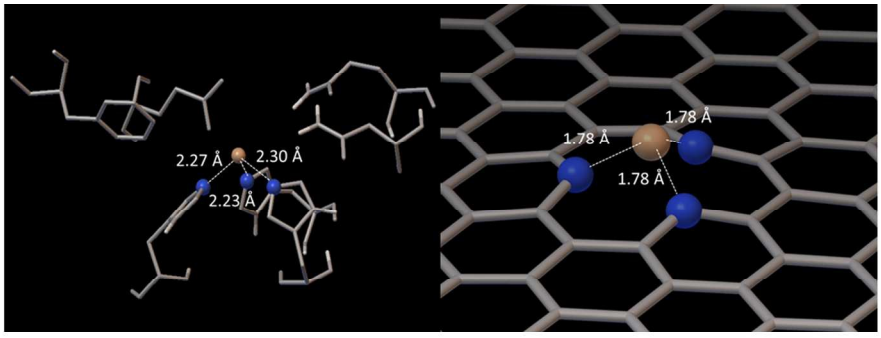

Figure 5: Left: Putative active site of *H. vulgare* oxalate oxidase (PDB 1FI2). Right: DFT optimized geometry of MnN_3 site in MnAAPyr. The nitrogen and manganese atoms are intentionally marked as blue and light brown spheres.

Journal Name RSCPublishing

ARTICLE

To gain a better understanding of the reactivity of MnAAPyr we further studied the mechanism of oxalate oxidation on the proposed active sites of the catalyst. Generally the reaction mechanism of oxalate oxidation on metallic surfaces can be divided into three different types, depending on the source of electrons[15, 55]. We considered the mechanism in which two electrons are transferred directly from oxalic acid molecule to the catalyst surface:

$$\begin{aligned} C_2O_4H_2 &\rightarrow * C_2O_4H + H^+ + e^- \\ &\rightarrow CO_2H * + CO_2 + H^+ + e^- \\ &\rightarrow 2CO_2 + 2H^+ + 2e^- \end{aligned} \quad (9)$$

where * represents the active site on the catalyst's surface. Other proposed mechanisms involve participation of another adsorbed species such as OH or O. Although co-adsorption of species such as OH, O, or H_2O and $C_2O_4H_x$ is plausible especially on the under-coordinated manganese in MnN_3 sites, they were not a part of the current study.

Free energy diagrams for the oxidation of oxalic acid on MnN_4, MnN_3C, MnN_2C_2, $MnN_2C_2(2)$ and MnN_3 sites at pH=4 are shown in Figure 6, and the electron energy and free energy changes for each of the steps are given in the Supplemental Material. The first step in the proposed mechanism is the adsorption of oxalic acid, which is accompanied by a release of H^+ and transfer of one electron to the electrode[55]. Gibbs free energy change for this step at U = 0 V was calculated as 1.14 eV, 0.64 eV, 0.40 eV, 0.71 eV and -1.14 eV for MnN_4, MnN_3C, MnN_2C_2, $MnN_2C_2(2)$ and MnN_3 sites, respectively.

For all the studied sites except for the MnN_3, the first step in the mechanism requires the largest change in the free energy and can be considered as thermodynamically limiting step. However, calculated energy changes shown on Figure 6 are valid only under open circuit conditions (U = 0 V) and will change as a response to an applied potential U. According to Eq. (8), applying potential will decrease the free energy change in each of the steps involving electron transfer by changing the chemical potential of the electron[42, 43], which will result in a decrease of the free energy required for the rate limiting step. For example, at the potential of +1.14 V vs. SHE the free energy change for the first step in the mechanism of oxalate oxidation will become zero on the MnN_4 site. This value gives us an estimate for the lower limit of the applied potential needed to drive the oxidation of oxalate acid on the different active sites. Consequently, based on the free energy diagrams on Figure 6, at the MnN_3C, MnN_2C_2, and $MnN_2C_2(2)$ sites oxidation of oxalic acid will run at potentials higher than 0.64 V, 0.40 V, and 0.71 V vs. SHE. Based on these results, MnN_2C_2 site will be the most active site, followed by MnN_3C, $MnN_2C_2(2)$, and MnN_4 site. Experimentally observed onset potential for oxalate oxidation, which was measured at 0.714 V vs. SHE, agrees well with the values calculated for MnN_3C and $MnN_2C_2(2)$ sites. This indicates that these sites are probably the ones responsible for the measured onset potential of MnAAPyr. Onset potential calculated for MnN_2C_2 on the other hand is much lower than the one measured for MnAAPyr, which implies that this site is probably the least occurring site in MnAAPyr. This agrees well with the calculated formation energies, which showed that among MnN_4, MnN_3C, MnN_2C_2, $MnN_2C_2(2)$ active sites,

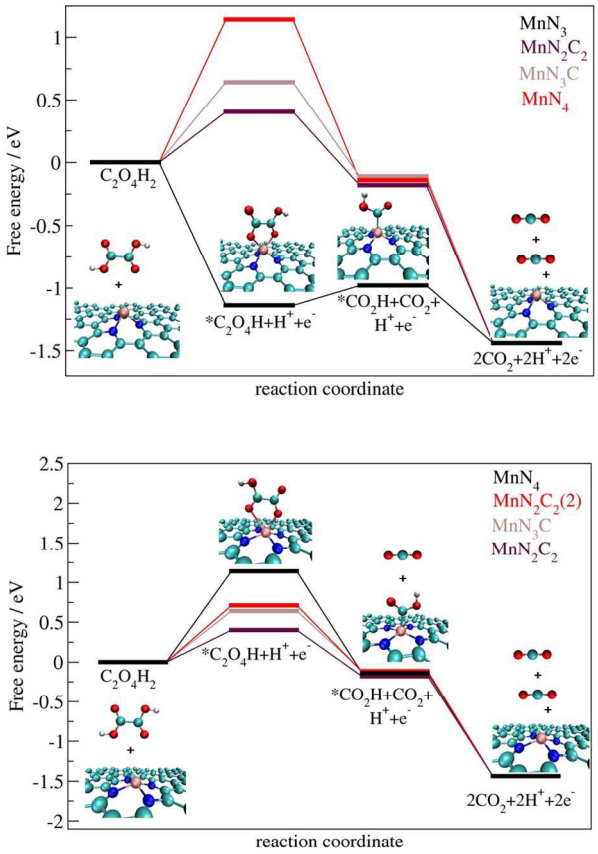

Figure 6. Free energy diagrams for oxalate oxidation on MnN_4, MnN_3C, MnN_2C_2, MnN_2C_2 (2), and MnN_3 sites at pH=4 and U=0 V.

MnN_2C_2 site is the least stable site. However, note that the calculated onset potentials represent the lower limit of the expected experimental onset potential for MnAAPyr as the calculated energy profiles do not include transition states.

The MnN_3 site on the other hand has a very different Gibbs free energy profile than the other sites. As seen from Figure 6, the step in oxalate oxidation mechanism that requires the largest change in the free energy is the cleavage of C-C bond in the adsorbed $*C_2O_4H$ species, which results in the formation of adsorbed $*CO_2H$ and gas

CO_2. As compared to other MnAAPyr active sites, adsorption of the oxalic acid and the first H^+/e- transfer step is exothermic on MnN_3 site with the change in the free energy of -1.14 eV. If we assume that the last two steps in the mechanism (cleavage of C-C bond in adsorbed $*C_2O_4H$ and the second $H^+\backslash e^-$ transfer) can be distinguished, the thermodynamically limiting step for MnN_3 site would then be the C-C bond breaking step with the energy change of 0.16 eV. Distinction between the MnN_3 site and other proposed sites can already be noticed when comparing adsorption energies of oxalic acid and oxalate anions $C_2O_4H^-$ and $C_2O_4^{2-}$ (Table 3). Oxalic acid and both oxalate anions have the highest affinity for MnN_3 site. For example, adsorption energies for $C_2O_4H^-$ are calculated as -2.34 eV, -2.78 eV, -3.12 eV, -2.82 eV and -4.56 eV on MnN_4, MnN_3C, MnN_2C_2, $MnN_2C_2(2)$ and MnN_3 site, respectively. High stability of adsorbed $C_2O_4H^-$ anion on under-coordinated Mn in the MnN_3 site explains why the first step in the oxalate oxidation mechanism is thermodynamically favorable on this site, while the second C-C breaking step is slightly unfavorable. In order to make both steps thermodynamically favorable, the optimal active site for oxalate oxidation would, thus, have adsorption energy for $C_2O_4H^-$ anion somewhere between -3.12 eV, which was calculated for MnN_2C_2 site, and -4.56 eV, calculated for MnN_3 site.

Table 3. Adsorption energies for oxalic acid and oxalate anions $C_2O_4H^-$ and $C_2O_4^{2-}$ on proposed active sites of MnAAPyr. Two configurations are considered: one in which oxygen atoms from the same carboxylic group are coordinated to Mn (config1) and the other in which both carboxylic groups are coordinated to Mn (config2). Configuration 2 for MnN_3 site is shown on Figure 7 and the rest are shown in the Supplemental Material.

Site	Adsorption energies /eV		Adsorption energies /eV		Adsorption energies /eV	
	$C_2O_4H_2$		$C_2O_4H^-$		$C_2O_4^{2-}$	
	config1	config2	config1	config2	config1	config2
MnN_4	-0.21	-0.02	-2.34	-2.28	-2.38	-3.27
MnN_3C	-0.29	-0.02	-2.78	-2.65	-2.87	-3.51
MnN_2C_2	-0.58	-0.13	-3.12	-3.02	-3.27	-4.09
$MnN_2C_2(2)$	-0.33	-0.29	-2.82	-2.71	-3.00	-3.91
MnN_3	-1.14	-1.21	-4.41	-4.56	-5.00	-6.37

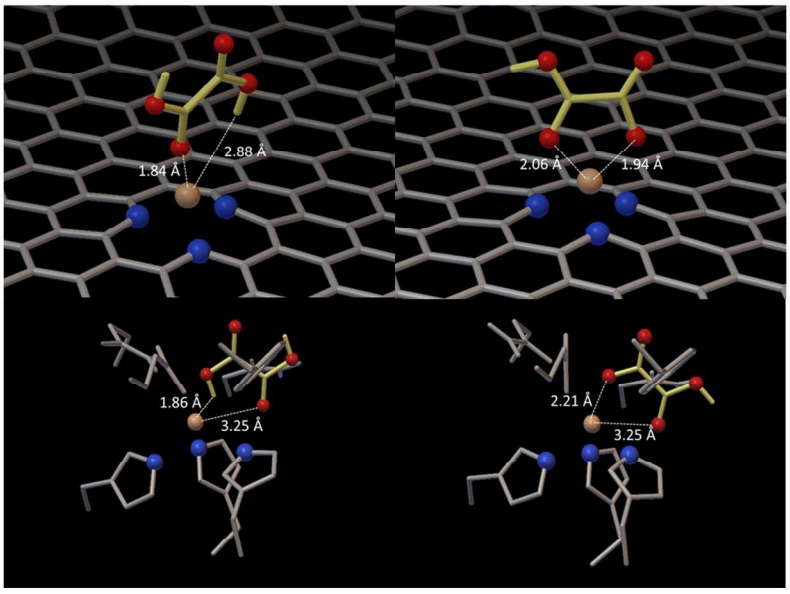

Figure 7: Optimized geometries of oxalic acid (upper left) and $C_2O_4H^-$ anion (upper right) adsorbed on MnN_3 active center and docking of oxalic acid (bottom right) and oxalate anion (bottom left) into OxOx obtained with AutoDock Vina 4.

As discussed previously, optimized geometry of MnN_3 active site shows features similar to the active site of OxOx and OxDc. Namely, in MnN_3 manganese atom is coordinated by three nitrogen atoms in a similar fashion as Mn atom in OxOx (Fig. 5). However, if we compare the binding of oxalic acid and $C_2O_4H^-$ anion on MnN_3 in MnAAPyr and OxOx's active site (Fig. 7), some differences can be observed. Besides different orientations of oxalic acid and oxalate anion on the enzyme's and MnAAPyr active sites, both oxalic acid and oxalate ion adsorb more strongly on MnN_3 site than in the active site of the enzyme, which is reflected in shorter distances between the oxalic acid or oxalate ion and the metal center in MnN_3 site as compared to the enzyme's active center. For instance, both oxygen atoms of the $C_2O_4H^-$ coordinate Mn atom in MnN_3 site with Mn-O distances being 2.06 Å and 1.94 Å, respectively. In OxOx active center, oxalate ion positions itself with only one oxygen atom towards the metal atom and the Mn-O distances are calculated as 2.21 Å and 3.25 Å, respectively. In the absence of oxalic acid Mn atom in OxOx is coordinated by three nitrogen atoms from His 88, His 90, His 137, and three oxygen atoms from Glu 95 and two water molecules. Thus, our results would suggest that when binding to Mn atom in OxOx, oxalate ion replaces one water molecule in the coordination shell of the metal center, while the other water molecule remains bound to the metal. This agrees well with the hypothesis that one water molecule stays coordinated to Mn and participates in the mechanism of oxalate oxidation in OxOx[16].

In conclusion, although there are some differences between the active centers of the enzymes capable of efficient oxidation of oxalic acid and the material synthetized in this study, using Mn coordinated with nitrogen incorporated in the carbon matrix has proven to be a successful approach in designing cheap non-PGM catalyst for oxalate oxidation.

Conclusions

We report a novel non-PGM catalyst MnAAPyr that is inspired by the structure of the active site of the Mn-dependent enzyme, oxalate oxidase. This new type of catalysts shows electrochemical activity towards oxidation of oxalic acid comparable to Pt. The oxalate oxidation on MnAAPyr has an onset potential measured at 0.714 ± 0.002 V vs. SHE at pH=4. The material has been synthesized using Sacrificial Support Method with manganese nitrate and 4-aminoantipyrine as precursors, and along with the low cost, its main advantage is the high catalytic surface area. The main features of the catalyst's active sites are similar to the active centers of naturally occurring enzymes that are capable of efficient and selective oxidation of oxalic acid. Namely, XPS studies show high abundance of of pyridinic, Mn–Nx, and pyrrolic nitrogen pointing towards the conclusion that nitrogen atoms coordinated to metal and pyridinic nitrogen constitute the active centers. We further used DFT in plane wave formalism with PBE functional to study the stability and activity of different one-metal active centers that could exist in the MnAAPyr catalyst. Based on the calculated formation energies, sites in which Mn is coordinated with four nitrogen atoms or three nitrogen atoms and one carbon atom in the square planar coordination are the most stable Mn-N_x sites and are, thus, the most abundant sites in our material. The onset potentials, which were calculated based on the free energy diagrams for oxalate oxidation mechanism on the different active centers of MnAAPyr show that MnN_3C and one of the MnN_2C_2 sites could be responsible for the experimentally observed onset potential of oxalate oxidation on MnAAPyr. Namely, lower limit of oxalate oxidation onset potentials for MnN_3C and MnN_2C_2 sites were calculated as 0.640 V and 0.710 V vs. SHE, which agrees well with the measured onset potential of 0.714 V vs. SHE.

Acknowledgements

This work was supported by US DOD, **ARO-Multi-University Research Initiative** grant W911NF-14-1-0263 to University of Utah. VASP license was provided by Theoretical division, LANL, which is supported by the Office of Science of the U.S. Department of Energy under Contract No. DE-AC52-06NA25396. Computational work was performed using the computational resources of **EMSL**, a national scientific user facility sponsored by the Department of Energy's Office of Biological and Environmental Research and located at Pacific Northwest National Laboratory, **NERSC**, supported by the Office of Science of the U.S. Department of Energy under Contract No. DE-AC02-05CH11231, and **CNMS**, sponsored at Oak Ridge National Laboratory by the Scientific User Facilities Division, Office of Basic Energy Sciences, U.S. Department of Energy. This paper has been designated LA-UR-14-29700.

Notes and references

[a] Chemical and Biological Engineering Department
Center for Micro-Engineered Materials (CMEM)
University of New Mexico, Albuquerque, NM 87131
[b] Theoretical Division, Los Alamos National Laboratory, Los Alamos, NM 87545

1. S. Roy, M. Vashishtha and A. K. Saroha, *J. Eng. Sci. Technol. Rev.*, 2010, **3**, 95-107.
2. Q. A. Acton, *Dicarboxylic Acids - Advances in Research and Application*, Scholarly Editions, Atlanta, Georgia, 2013.
3. S. R. Khan, *Calcium Oxalate in Biological Systems*, CRC Press. Inc., Roca Raton, Florida, 1995.
4. C. Santoro, A. Serov, C. W. Villarrubia, S. Stariha, S. Babanova, A. J. Schuler, K. Artyushkova and P. Atanassov, *ChemSusChem*, 2014, Accepted.
5. U. Martinez, A. Serov, M. Padilla and P. Atanassov, *ChemSusChem*, 2014, **7**, 2351-2357.
6. A. Serov, U. Martinez, A. Falase and P. Atanassov, *Electrochem. Commun.*, 2012, **22**, 193-196.
7. A. Serov, U. Martinez and P. Atanassov, *Electrochem. Commun.*, 2013, **34**, 185-188.
8. A. Zalineeva, A. Serov, M. Padilla, U. Martinez, K. Artyushkova, S. Barton, C. Coutanceau and P. Atanassov, *J. Am. Chem. Soc*, 2014, **136**, 3937-3945.
9. S. Imamura, *Ind. Eng. Chem. Res.*, 1999, **38**, 1743-1753.
10. Y. Matatov-Meytal and M. Sheintuch, *Ind. Eng. Chem. Res.*, 1998, **37**, 309-326.
11. D. Duprez, F. Delanoë, J. Barbier Jr., P. Isnard and G. Blanchard, *Catal. Today*, 1996, **29**, 317-322.
12. P. Gallezot, N. Laurain and P. Isnard, *Appl. Catal., B*, 1996, **9**, L11-L17.
13. P. Gallezot, S. Chaumet, A. Perrard and P. Isnard, *J. Catal.*, 1997, **168**, 104-109.

14. N. I. Andersen, A. Serov and P. Atanassov, *Appl. Catal. B: Environmental*, 2014, DOI: 10.1016/j.apcatb.2014.08.033.
15. M. J. Chollier, F. Epron, L.-P. E. and J. Barbier, *Catal. Today*, 1999, **48**, 291-300.
16. D. Svedružić, S. Jonsson, C. G. Toyota, L. A. Reinhardt, S. Ricagno, Y. Lindqvist and N. G. J. Richards, *Arch. Biochem. Biophys.*, 2005, **433**, 176-192.
17. H. Koyama, *Agric. Biol. Chem.*, 1988, **53**, 743-748.
18. E.-J. Woo, J. M. Dunwell, P. W. Goodenough, A. C. Marvier and R. W. Pickersgill, *Nature Structural Biology* 2000, **7**, 1036-1040.
19. H. Luckarift, P. Atanassov and G. Johnson, *Enzymatic fuel cells: From fundamentals to applucations*, John Wiley and Sons, Inc., Hoboken, New Jersey, 2014.
20. G. Strack, S. Babanova, K. E. Farrington, H. R. Luckarift, P. Atanassov and G. R. Johnson, *J. Electrochem. Soc.*, 2013, **160**, G3178-G3182.
21. A. Serov, K. Artyushkova and P. Atanassov, *Adv. Energy Mater.*, 2014, **4**, 1301735.
22. K. Artyushkova, C. Walker, W. Patterson and P. Atanassov, *Electrocatalysis*, 2014, **5**, 241-245.
23. S. Brocato, A. Serov and P. Atanassov, *Electrochim. Acta*, 2013, **87**, 361– 365.
24. M. H. Robson, A. Serov, K. Artyushkova and P. Atanassov, *Electrochim. Acta*, 2013, **90**, 656– 665.
25. S. Pylypenko, S. Mukherjee, T. S. Olson and P. Atanassov, *Electrochim. Acta*, 2008, **53**, 7875–7883.
26. U. Tylus, Q. Jia, K. Strickland, N. Ramaswamy, A. Serov, P. Atanassov and S. Mukerjee, *J. Phys. Chem. C*, 2014, **118**, 8999-9008.
27. A. Serov, M. Padilla, J. A. Roy, P. Atanassov, T. Sakamoto and K. Asazawa, *Angew. Chem. Int. Ed.*, 2014, 126, 10419-10715.
28. A. Serov, A. Aziznia, P. H. Benhangi, K. Artyushkova, P. Atanassov and E. Gyenge, *J. Mater. Chem. A*, 2013, **1**, 14384-14391.
29. J. P. Perdew, K. Burke and M. Ernzerhof, *Phys. Rev. Lett.*, 1996, **77**, 3865-3868.
30. J. P. Perdew, K. Burke and M. Ernzerhof, *Phys. Rev. Lett.*, 1997, **78**, 1396-1396.
31. P. E. Blöchl, *Phys. Rev. Lett.*, 1994, **50**, 17953-17979.
32. G. Kresse and J. Joubert, *Phys. Rev. B.*, 1999, **59**, 1758-1775.
33. G. Kresse and J. Hafner, *Phys. Rev. B.*, 1993, **47**, 558-561.
34. G. Kresse and J. Hafner, *Phys. Rev. B.*, 1994, **49**, 14251-14269.
35. G. Kresse and J. Furthmüller, *Comput. Mat. Sci.*, 1996, **6**, 15-50.
36. G. Kresse and J. Furthmüller, *Physical Review B*, 1996, **54**, 11169-11186.
37. H. J. Monkhorst and J. D. Pack, *Phys. Rev. B: Condens. Matter Mater Phys.*, 1976, **13**, 5188-5192.
38. P. E. Blöchl, O. Jepsen and O. K. Andersen, *Phys. Rev. B: Condens. Matter Mater Phys.*, 1994, **49**, 16223-16233.
39. P. Trucano and R. Chen, *Nature*, 1975, **258**, 136-137.
40. A. F. Kohan, G. Ceder, D. Morgan and C. G. Van de Walle, *Phys. Rev. B:*, 2000, **61**, 15019-15027.
41. P. W. Atkins, *Physical Chemistry*, Oxford University Press, Oxford, 1998.
42. J. K. Nørskov, J. Rossmeisl, A. Logadottir, L. Lindqvist, J. R. Kitchin, T. Bligaard and H. H. Jónson, *J. Phys. Chem. B.*, 2004, **108**, 17886-17892.
43. J. Rossmeisl, A. Logadottir and J. K. Nørskov, *Chem. Phys.*, 2005, **319**, 178-184.
44. O. Trott and A. J. Olson, *J. Comput. Chem.*, 2009, **31**, 455-461.
45. M. J. Frisch, G. W. Trucks, H. B. Schlegel, G. E. Scuseria, M. A. Robb, J. R. Cheeseman, G. Scalmani, V. Barone, B. Mennucci, G. A. Petersson, H. Nakatsuji, M. Caricato, X. Li, H. P. Hratchian, A. F. Izmaylov, J. Bloino, G. Zheng, J. L. Sonnenberg, M. Hada, M. Ehara, K. Toyota, R. Fukuda, J. Hasegawa, M. Ishida, T. Nakajima, Y. Honda, O. Kitao, H. Nakai, T. Vreven, J. A. Montgomery, J. E. P. Jr., F. Ogliaro, M. Bearpark, J. J. Heyd, E. Brothers, K. N. Kudin, V. N. Staroverov, R. Kobayashi, J. Normand, K. Raghavachari, A. Rendell, J. C. Burant, S. S. Iyengar, J. Tomasi, M. Cossi, N. Rega, J. M. Millam, M. Klene, J. E. Knox, J. B. Cross, V. Bakken, C. Adamo, J. Jaramillo, R. Gomperts, R. E. Stratmann, O. Yazyev, A. J. Austin, R. Cammi, C. Pomelli, J. W. Ochterski, R. L. Martin, K. Morokuma, V. G. Zakrzewski, G. A. Voth, P. Salvador, J. J. Dannenberg, S. Dapprich, A. D. Daniels, Ö. Farkas, J. B. Foresman, J. V. Ortiz, J. Cioslowski and D. J. Fox, Gaussian, Inc., Wallingford CT, 2009.
46. K. Artyushkova, B. Kiefer, B. Halevi, A. Knop-Gericke, R. Schloglc and P. Atanassov, *ChemComm*, 2013, **49**, 2539-2541.
47. L. C. Rockombeny, J. P. Féraud, B. Queffelec, D. Ode and T. Tzedakis, *Electrochim. Acta*, 2012, **66**, 230-238.
48. K. S. Yamaguchi and D. T. Sawyer, *Isr. J. Chem.*, 1985, **25**, 164-176.
49. D. K. Cha and S.-M. Park, Proceedings of the 1996 Hazardous Substance Research Center/Waste-management Education and Research Consortium joint conference on the environment, Bozeman, MT, USA, 1994.
50. A. Bern, A. Rodes and J. M. Feliu, *J. Electroanal. Chem.*, 2004, **563**, 49-62.
51. D. Svedruzic, S. Jonsson, C. G. Toyota, L. A. Reinhardt, S. Ricagno, Y. Lindqvist and N. G. J. Richards, *Archives of Biochemistry and Biophysics*, 2005, **433**, 176–192.
52. S. P. Kattel, B. Kiefer and P. Atanassov, *ECS Trans.*, 2010, **55**, 5552.
53. S. Kattel, P. Atanassov and B. Kiefer, *J. Phys. Chem. C*, 2012, **116**, 8161-8166.
54. R. Faccio, L. Fernández-Werner, H. Pardo, C. Goyenola, O. N. Ventura and Á. I. W. Mombrú, *J. Chem. Phys. C*, 2010, **114**, 18961.
55. J. W. Johnson, H. Wroblowa and O. M. Bockris, *Electrochim. Acta*, 1964, **9**, 639-651.

Journal Name

RSCPublishing

ARTICLE

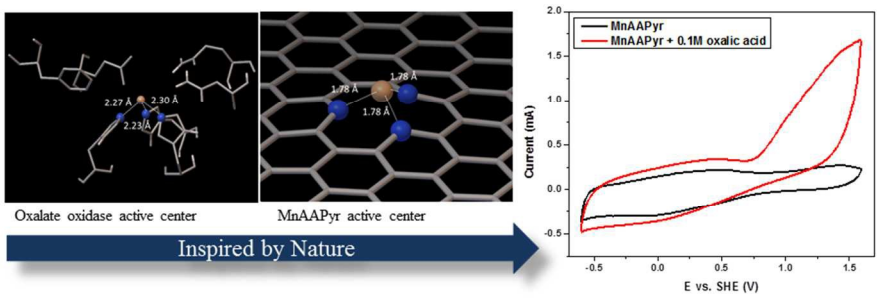

Table of contents: A novel non-PGM MnAAPyr catalyst that shows electrochemical activity towards oxidation of oxalic acid comparable to Pt.